Use of Modern Non-destructive Techniques in High Temperature Degradation of Material and Coatings

C. K. Lee and Y. H. Sohn

Abstract

The durability and reliability of thermal barrier coatings (TBCs) play an important role in the service reliability, availability and maintainability (RAM) of hot-section components in advanced turbine engines for aero and utility applications. Photostimulated luminescence spectroscopy (PSLS) and electrochemical impedance spectroscopy (EIS) are being concurrently developed as complimentary non-destructive evaluation (NDE) techniques for quality control and life-remain assessment of TBCs. This paper overviews the governing principles and applications of the luminescence and the impedance examined in the light of residual stress, phase constituents and resistance (or capacitance) in TBC constituents including the thermally grown oxide (TGO) scale. Results from NDE by PSLS and EIS are discussed and related to the microstructural development during high temperature thermal cycling, examined by using a variety of microscopic techniques including focused ion beam (FIB) in-situ lift-out (INLO), transmission and scanning transmission electron microscopy (TEM and STEM).

Key Words : Thermal barrier coatings, Non-destructive evaluation, Photostimulated luminescence, Electrochemical impedance, Transmission electron microscopy, Focused ion Beam, microstructure.

1. Introduction

Thermal barrier coatings (TBCs) consisting of 7~8 wt.% Y_2O_3 stabilized ZrO_2 (YSZ), applied by air plasma sprayed (APS) or electron-beam physical vapor deposition (EBPVD), play a critical role in the performance and reliability of modern gas turbine engines [1~4]. The YSZ coatings are deposited on hot-section components (e.g., combustors, vanes and blades) of the turbine engines; they provide a thermal gradient between the hot exhaust gas and the superalloy surface owing to their low thermal conductivity. The high temperature thermodynamics and kinetics of the TBC are of particular interest since oxygen diffuses through the ceramic coating and oxidizes the alumina-forming MCrAlY (M=Ni and/or Co) or (Ni,Pt)Al bondcoats, which is an intermediate coating layer between the YSZ and the superalloy. As a result of oxidation, the thermally grown oxide (TGO), consisting primarily of α-Al2O3, forms and grows with associated growth stresses. In addition, TBCs are subject to stresses during thermal cycling due to the thermal expansion mismatch between the metallic substrate and the ceramic coatings. Generally, damage from thermal cyclic exposure initiates at multiple interfacial flaws in the vicinity of the TGO. These flaws link with continued cycling and the TBCs fail by the spallation of the TGO and/or YSZ coating, leaving the oxidation resistant bond coat on the component exposed to higher than designed temperatures that lead accelerated degradation.

C. K. Lee : Department of Mechanical Engineering, Seoul National University of Technology, Seoul, Korea
E-mail : chullee@snut.ac.kr
Y. H. Sohn : Advanced Materials Processing and Analysis Center (AMPAC), University of Central Florida, Orlando, U.S.A.
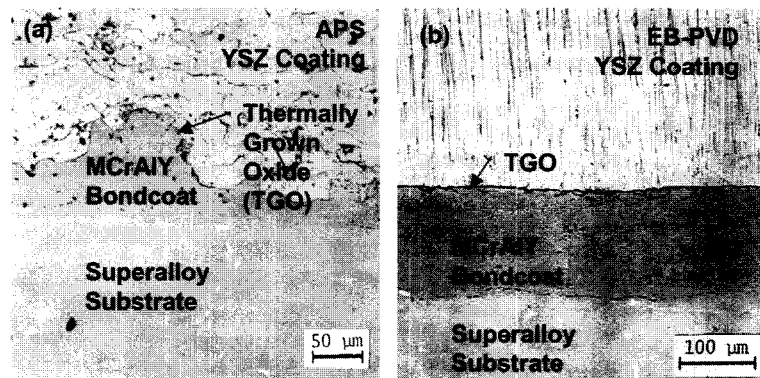E-mail : ysohn@mail.ucf.edu

Fig.1 Backscattered electron micrographs of the (a) air plasma sprayed
and (b) electron beam physical vapor deposited thermal barrier coatings (TBCs).

Backscattered electron micrographs of the typical APS and EB-PVD TBCs are presented in Fig. 1.

Since the failure of TBC frequently involves component failure and unscheduled maintenance of gas turbine engines, it is important that the integrity of TBCs be non-destructively evaluated by examining the characteristics of TBCs including residual stress, thickness and the phase constituents of TGO, as well as presence of any subcritical damage during thermal cycling. The non-destructive evaluation (NDE) of these characteristics can provide critical information regarding the damage/failure mechanisms of TBCs and can be a part of parameters monitored for lifetime management of TBCs and engine operation.

In addition, mechanism-based life prediction model of TBCs require refined understanding of failure mechanisms associated with the spallation of coatings based on detailed microstructural analysis. Until recently, microstructural analysis of TBCs has been limited to x-ray diffraction (XRD) and scanning electron microscopy (SEM). Investigation of microstructure at high resolution using TEM and STEM was rare since specimen preparation of thermally cycled TBCs has been impracticable due to extreme fragile nature of specimens with multiple interfaces.

This paper first introduces the fundamentals principles governing two developmental NDE techniques, namely photostimulated luminescence spectroscopy (PSLS) [5~12] and electrochemical impedance spectroscopy (EIS) [13~15]. Selected results of

PSLS and EIS are highlighted with respect to the TBC failure in the light of lifetime prediction and life-remain assessment. This paper, in addition, illustrates TBC specimen preparation for TEM analysis by recently refined technique, focused ion beam (FIB) in-situ lift-out (INLO). Selected microstructural observations, carried out by TEM and STEM via FIB-INLO specimen preparation, are highlighted with respect to better understanding of TBC failure.

2. Photostimulated luminescence spectroscopy (PSLS)

The Cr^{3+} photoluminescence in α-Al_2O_3 occurs by the photon emission from the excitation and subsequent relaxation of electrons in substitutional impurity Cr^{3+} ions in α-Al_2O_3 lattice [5~12]. Two distinct fluorescence transitions are allowed by the crystal field symmetry of the Cr^{3+} site in stress-free α-Al_2O_3 crystals, corresponding to the R_1 and R_2 fluorescence doublets occurring at frequencies of 14,402 and 14,432 cm^{-1}, respectively. However, when the crystal is strained, the crystal field about the Cr^{3+} ion is perturbed and the R-lines exhibit a systematic shift, known as the piezospectroscopic effect. For polycrystalline α-Al_2O_3, such as in TGO, the Cr^{3+} photoluminescence also depends on crystallographic orientation, grain size, and grain shape distributions [5~7]. The frequency shift, $\overline{v}$, of R_1 and R_2 luminescence
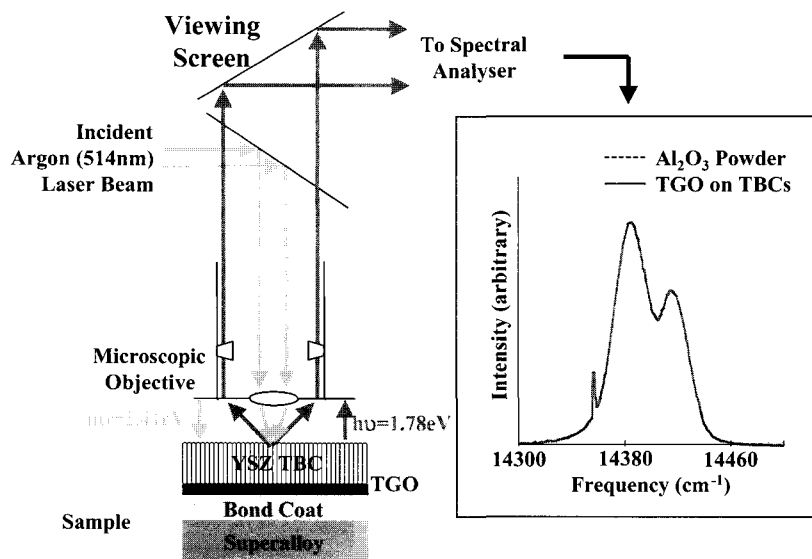
Fig. 2 Non-destructive evaluation of the thermally grown oxide (TGO) in TBCs
by photostimulated luminescence spectroscopy (PSLS) technique

can be related to the average stress, $\bar{\sigma}$ of the α -Al₂O₃ by:

$$\triangle \bar{\nu} = \frac{2}{3} \Pi \bar{\sigma} \qquad (1)$$

where Π is the coefficient of the piezo-spectroscopic tensor (a material specific parameter that reflects the point symmetry of the fluorescing ion in the host lattice). The overall residual stress within the TGO can be calculated from the position of the luminescence peaks and the measured values of piezo-pectroscopic tensor, assuming a thin, randomly oriented polycrystalline and biaxially stressed α -Al₂O₃ [5~7]. Photo-stimulated luminescence from metastable phases of Al₂O₃ including γ and θ phases has been observed [8,9]. In addition, Cr^{3+} concentration in α -Al₂O₃ has been reported to influence the magnitude of the luminescence shifts [10].

The PSLS technique for TBCs works because of the transparency of the YSZ coating at optical frequencies. This allows the luminescence from TGO, buried underneath YSZ coating. Despite the porosity and grain boundary scattering, the YSZ coatings are partially translucent since the optical band gap of partially stabilized zirconia is approximately 12 eV - well above the energy of either those of incident argon

-ion lasers (514 and 488 nm) or the characteristic ruby R-line fluorescence from Cr^{3+} ions in aluminum oxide (693 nm). When the coatings are illuminated using an argon ion laser, characteristic ruby R-line fluorescence from Cr^{3+} ions in alumina can be detected quickly with good signal to noise ratio. A schematic of the PSLS technique is shown in Fig. 2, illustrating the incident laser beam and the resulting fluorescence from the TGO, which gives rise to a photo-luminescence spectrum. The shift in the luminescence then can be used for the calculation of residual stress in the α -Al₂O₃ TGO using Eq. (1).

The non-destructive, non-contact nature of the PSLS makes it a very attractive tool for monitoring the life of TBCs [11,12]. Several parameters of luminescence spectra have been identified to evolve during high temperature exposure of TBCs. These include (1) the piezo-spectroscopic shift (i.e., TGO residual stress), (2) broadening and/or bimodal luminescence of α -Al₂O₃ (and the corresponding deconvolution procedure / routine), and (3) luminescence from metastable γ - and θ -Al₂O₃ phases. These parameters, as envisaged by Clarke [12], must be accurately correlated and understood in terms of microstructural development, damage evolution and failure mechanisms of TBCs, for successful development and implementation of PSLS as a NDE technique.
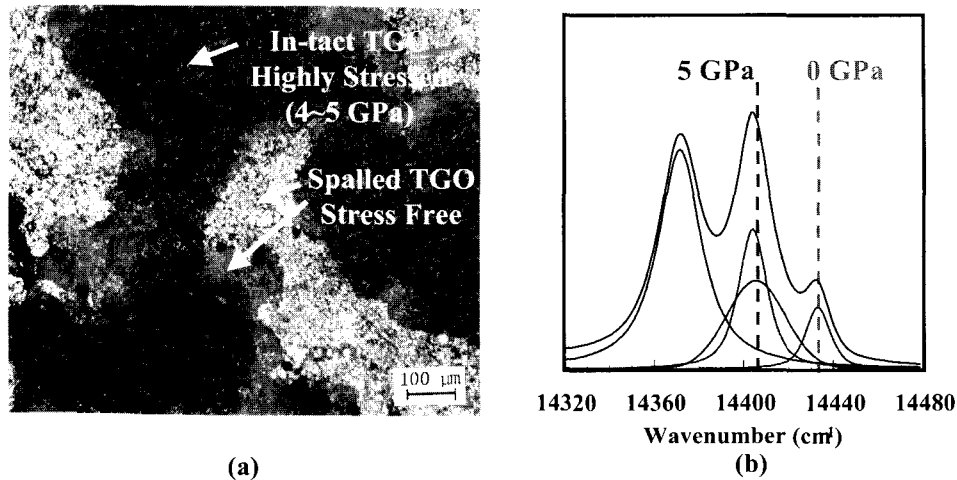
Fig. 3 Stress assessment of TBC by photo-stimulated luminescence spectroscopy :
(a) Top of NiCoCrAlY bond coat surface after the spallation of ZrO2-8wt.%Y2O3 coating, and
(b) Bimodal R1-R2 photoluminescence frequently observed due to the presence of intact and
stress-relieved thermally grown oxides on the bond coat surface

Clarke and coworkers [12] have reported that, after an initial transient period, compressive residual stress remains almost constant throughout the oxidation time. Prior to failure of TBCs, a slight decrease in the magnitude of compressive residual stress was observed in some instances. A similar observation was made by Sohn et al. [7] where a gradual decrease in the magnitude of compressive residual stress (along with increase in the standard deviation) was observed for some TBC specimens. However, in many other instances, the magnitude of compressive residual stress suddenly decreased along with TGO spallation and TBC failure. This abrupt relaxation of compressive residual stress within the TGO scale arise from the relief of stress arising from the CTE mismatch between the TGO and bond coats. For spalled TGO scales or TBCs, bimodal luminescence consisting of two sets of R_1-R_2 luminescence is frequently observed. In most instances, one set of R_1-R_2 luminescence corresponds to intact TGO (i.e., stressed/shifted luminescence) and the other to spalled TGO (i.e., nearly stress-free/no luminescence shift) as illustrated in Fig. 3. As for the slight decrease in the magnitude of compressive residual stress within TGO prior to the TBC failure, the cause is not yet fully understood.

Constant magnitude of compressive residual stress within the TGO during thermal exposure may be a characteristic of the mechanically stable TGO [7,12]. However, changes, especially the gradual decrease in the magnitude of compressive residual stress can be related to many phenomena of high temperature oxidation: TGO wrinkling or TGO rumpling or other stress relaxation mechanisms, possibly even micro-cracking. Magnitude of compressive residual stress within the TGO for a given TBC system can even vary. The broadening of the R_1-R_2 luminescence lines is frequently observed from intact TBC with intact (i.e., compressively stressed) TGO and can be attributed to the existence of strain gradients through the volume of TGO scale probed.

Although the evolution of bimodal luminescence can be considered as a critical parameter to monitor the integrity of TBCs, there exist another source of bimodal luminescence as reported by Clarke [12], and again confirmed by Sohn et al. [7]. While the equilibrium α-Al$_2$O$_3$ phase of the TGO with continuous morphology is constrained with respect to the CTE mismatch with the bond coat, the metastable phases such as γ- and θ-Al$_2$O$_3$, with whisker morphology, can be unconstrained. Presence of these metastable phases can also be detected by their unique luminescence using PSLS. During high temperature exposure, these metastable phases transform to the equilibrium α-Al$_2$O$_3$ and may give rise to the bimodal

R-luminescence from α-Al₂O₃, because its morphology dictate the residual stress based on CTE mismatch. The evolution of bimodal R-luminescence, in this case, depends on the rate of phase transformation and development of interface morphology (recession of whisker morphology by interphase boundary diffusion).
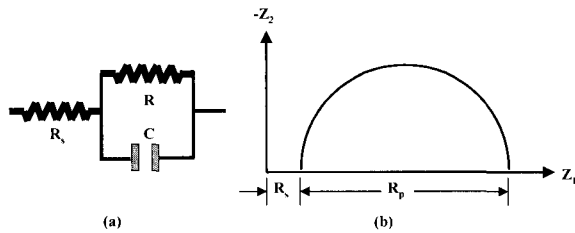

Fig. 4 (a) A simple AC circuit consisting of a resistance and a capacitance (b) and the corresponding Nyquist diagram for single time constant. RS refer to the resistance of the electrolyte solution in electrochemical impedance spectroscopy

3. Electrochemical impedance spectroscopy (EIS)

EIS is a NDE technique being developed to evaluate the microstructure, defects and degradation of TBCs by examining their electrochemical impedance response to an applied voltage in the range of 5-50 mV over a frequency range of 10 mHz - 1 MHz. The electrochemical impedance response is recorded in terms of impedance plots that contain information regarding the microstructural features of TBCs.

There are two types of impedance diagrams, namely Nyquist and Bode plots. In a Nyquist plot, the impedance is represented by a real part Z_1 and an imaginary part Z_2 according to the formula:

$$Z(\omega) = Z_1 - jZ_2 \qquad (2)$$

where $j = \sqrt{-1}$ and ω is the angular frequency. In a Bode plot, the logarithm of modulus of impedance Z and the phase angle θ are plotted as a function of frequency f. For a simple resistor-capacitor (R-C)

circuit connected in parallel as depicted in Fig. 4 (a), the Nyquist plot shows a semi-circle as presented in . 4 (b), which is characteristic of a single time constant, τ (τ = R·C). The resistance of electrolyte is represented as a resistor RS. In a Nyquist plot that consists of a single semicircle, the resistance R connected in parallel to the capacitor C can be directly determined from the intercept with the real axis (Z1). The impedance equation for the circuit presented in Fig. 4(a) can be expressed as:

$$Z(\omega) = \frac{R}{1 + \omega^2 C^2 R^2} - \frac{j\omega C R^2}{1 + \omega^2 C^2 R^2} \qquad (3)$$

where R and C are defined as:

$$R = \frac{\rho \cdot t}{A} \qquad (4)$$

$$C = \varepsilon_v \cdot \varepsilon \frac{A}{t} \qquad (5)$$

The variables ρ, t and ε refer to the electrical resistivity, thickness and dielectric constant, respectively of the material, ε_v is the dielectric constants of vacuum, and A is the surface area of the material exposed to the electrolyte. Electrochemical impedance response of material also depends on the parameters such as conductivity of the electrolyte and microstructural features of materials such as pores and defects.

For TBCs, the electrochemical impedance characteristic depends on the thickness and microstructure of the YSZ, the thickness and microstructure of the TGO, and potentially, the damages at critical interfaces in the vicinity of the TGO [13-15]. In general, a Nyquist plot from TBCs consists of three or four semi-circles corresponding to three or four time constants. Based on these time constants and the microstructural features of TBCs, AC equivalent circuits can be designed as presented in Fig. 5 and 6. Fig. 5 represents a typical as-coated APS TBC without the TGO and the corresponding AC equivalent circuit, which should give rise to three semi-circles in a Nyquist plot. The three time constants, accordingly, correspond to the YSZ topcoat layer ($R_{YSZ} \cdot C_{YSZ}$),

which has a frequency range of 0.3~0.6 MHz, the pores in the YSZ ($R_P \cdot C_P$) in the range of 1Hz, and the charge transfer resistance at the interface between the YSZ and bondcoat ($R_T \cdot C_T$) in the range of 100~200 Hz. The circuit for APS TBC consists of constant phase elements in the place of an ideal capacitor, because of the roughness of the YSZ surface and YSZ-bondcoat interfaces that give rise to frequency dispersion due to the non-uniform distribution in the current density [16,17]. Other features such as porosity, pore shape, and other defects can also contribute to the non-uniform distribution in the current density [16,17].

Fig. 6 represents a typical as-coated EB-PVD TBC with the TGO and the corresponding AC equivalent circuit, which should give rise to four semi-circles in a Nyquist plot. The four time constants, accordingly, correspond to the YSZ topcoat layer ($R_{YSZ} \cdot C_{YSZ}$), which has a frequency range of 1MHz~103 Hz, the pores in the YSZ ($R_P \cdot C_P$) in the range of~10 Hz, the TGO ($R_{TGO} \cdot C_{TGO}$) in the range of ~103 Hz, and the charge transfer resistance at the interface between the TGO and the bondcoat ($R_T \cdot C_T$) in the range of ~1 Hz. In the case of EB-PVD, the charge transfer resistance is masked in the frequency range between 1~10-2 Hz. The surface and interfaces in EB-PVD TBCs are typically smooth enough so that ideal capacitors are used.
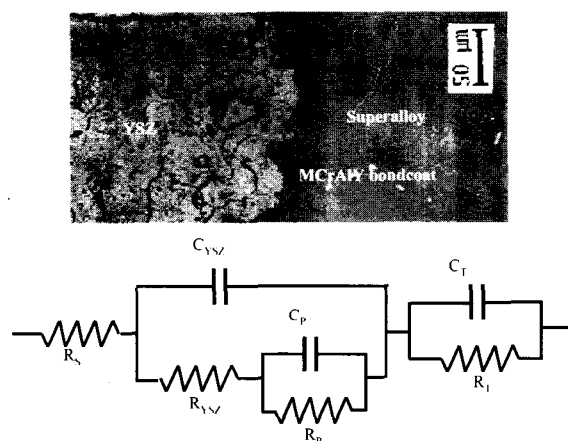

Fig. 5 A typical microstructure of air plasma sprayed TBCs and the corresponding AC equivalent circuit employed for electrochemical impedance spectroscopy
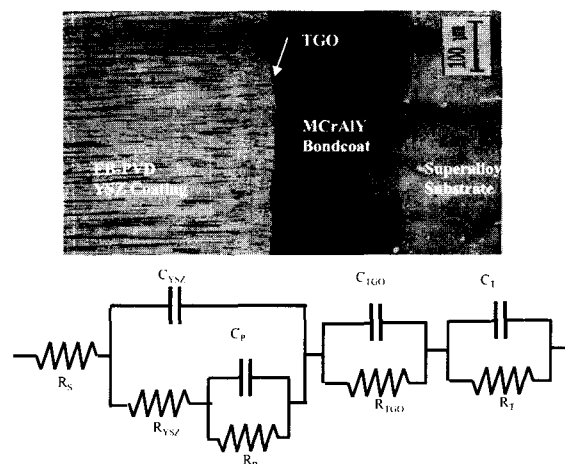

Fig. 6 A typical microstructure of electron beam physical vapor deposited TBCs and the corresponding AC equivalent circuit employed for electrochemical impedance spectroscopy

Fig. 7 represents a typical evolution in the resistance and capacitance of TBC constituents as a function of thermal cycling. In this study, five disks of EB-PVD TBCs specimens were thermally cycled at 1121°C with 10-minute heat-up, 40-minute dwell and 10-minute air-quench. EIS measurement was carried out for specimens with 0, 5, 50, 200 and 419 cycles. Spallation failure of TBC occurred at 419 cycles. In Fig. 7, there is an initial increase in the RYSZ and an initial decrease in the C_{YSZ} with thermal cycling. R_{TGO} and C_{TGO} also exhibit an initial increase and a decrease, respectively. These initial changes are attributed to sintering of YSZ coatings and growth of TGO (i.e., Al_2O_3) due to high temperature oxidation of bond coat. In fact, the thickness of TGO and the electrochemical capacitance of TGO was observed to be inversely related [13]. With further thermal cycling, a gradual decrease in R_{YSZ} and an abrupt increase in the C_{YSZ} were observed with TBC failure, Similarly, R_{TGO} decreased gradually and C_{TGO} increased abruptly. While these changes are gradual in the case of resistance and abrupt in the case of capacitance, both represent sub-critical damage (e.g., cracks and voids) through which conductive electrolyte can penetrate and make a contact with conductive metallic bond coat [13-15]. The effective number of cations in the electrolyte and anions from bond coat surface increases for free
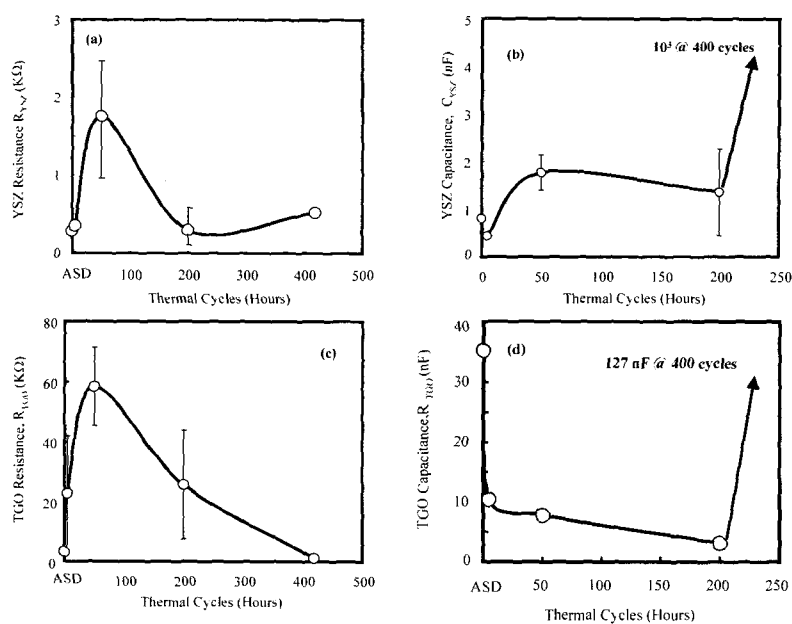
Figure 7. Typical variation in (a) resistance and (b) capacitance of YSZ and (c) resistance and (d) capacitance of TGO as a function of thermal cycling in air at 1121 °C for electron beam physical vapor deposited TBCs
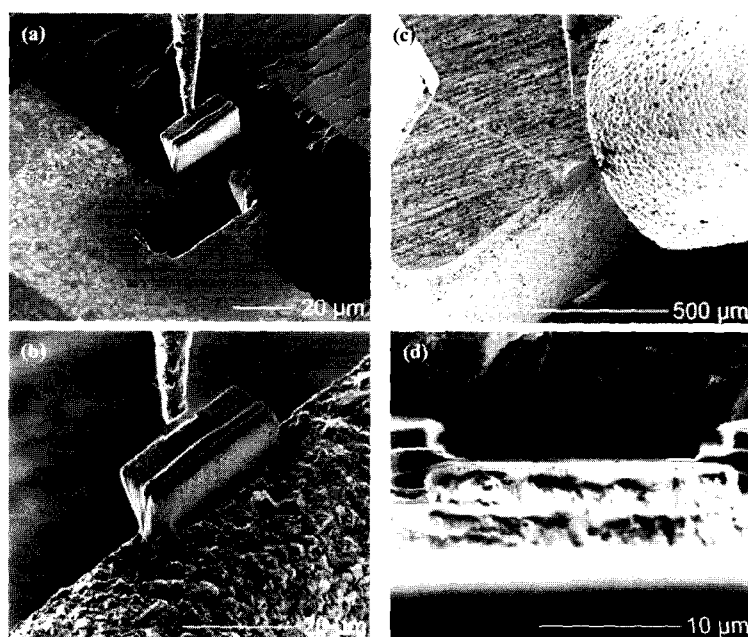

Fig. 8 Secondary electron focused ion beam (FIB) images showing sequence of the FIB in-situ lift-out (INLO) TEM specimen preparation process (a-d) for a representative TBC specimen.

conduction. These trends can be employed to non-destructively evaluate the integrity of TBCs. Consistent trends have been observed for many different TBCs with various thermal exposures. In addition, processing-dependent variation in the microstructure of TBCs has been distinguished by EIS [14].
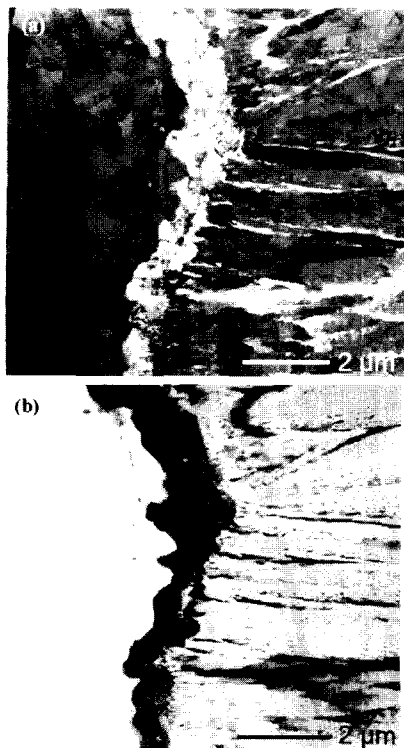
Fig. 9 Typical microstructure of as-coated TBC specimen in the vicinity of the thermally grown oxide: (a) bright-field image and (b) high angle annular dark field image

4. Focused ion beam (FIB) in-situ lift-out (INLO)

In preparing TEM specimens of TBCs using FIB-INLO, the cross-sectional samples are embedded in transparent cold-setting epoxy, and ground using 600-grit SiC paper, followed by polishing with diamond paste down to 1/4 μm. The polished surface of the specimens is then sputter coated with Au-Pd to create adequate conduction during FIB imaging and milling operations. A transmission electron microscopy (TEM) specimen is prepared from the cross-section utilizing the focused ion beam (FIB) in-situ lift-out (INLO) technique [18-20]. With the FIB technique, a wedge shaped sample is cut free from the bulk material by means of FIB milling. The sample is then attached to the in-situ W probe using ion beam assisted Pt

chemical vapor deposition (CVD) as shown in Fig. 8(a). Next, the ion beam assisted Pt CVD is used to attach the sample to a 2 mm x 1 mm Cu TEM grid that had been previously cut to accommodate access to the grid with the in-situ W probe as shown in Fig. 8(b). Once it is secured to the TEM grid, the sample is milled free from the in-situ W probe and then subsequently FIB milled to electron transparency (~100 nm) as shown in Fig. 8(c,d). Typically, this process takes approximately 3 hours per specimen.
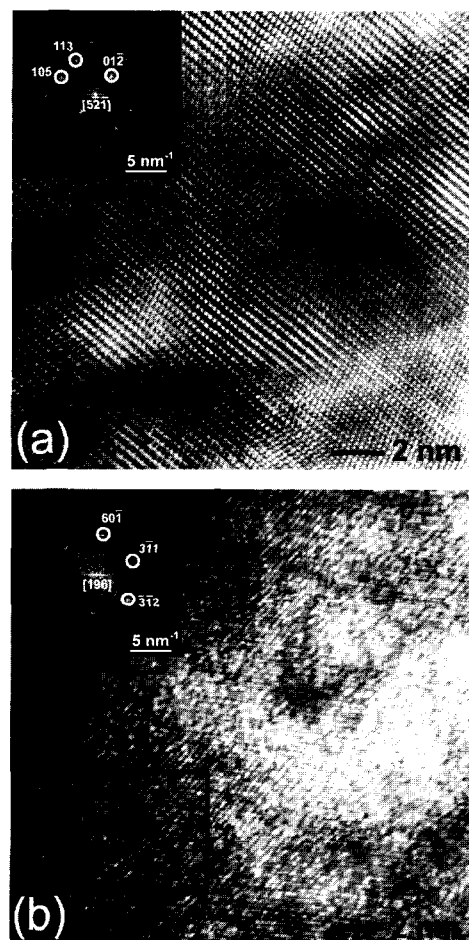

Fig. 10 Bright field high resolution TEM image with the corresponding fast-fourier transformed diffractogram from thermally grown oxide formed on TBC specimen in the as-coated bond coat where the indexed fast-fourier transformed diffractogram corresponds to (a) α -Al2O3 (hexagonal close packed) with a beam direction of [$5\bar{2}\bar{1}$] and (b) θ -Al2O3 (monoclinic) with a beam direction [196].

Fig. 11 Bright field TEM micrograph of intact electron beam physical vapor deposited TBC specimen after 645, 10-hour thermal cycles at 1038°C. Extensive decohesion at or near the YSZ/TGO interface was observed
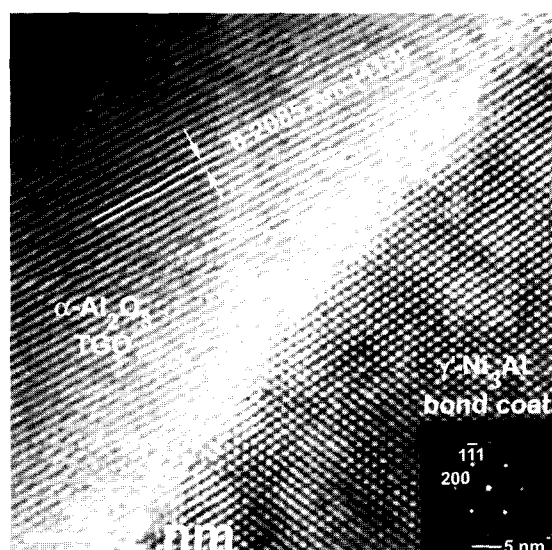

Fig. 12 High resolution BF image of the interface between TGO and (Ni,Pt)Al bond coat for the intact EB-PVD TBC specimen after 645, 10-hour thermal cycles at 1038°C. The FFT diffractogram (inset) from the bond coat corresponds to that of γ'-Ni3Al solid solution phase

5. Transmission and scanning transmission electron microscopy (TEM and STEM)

Once the TEM specimen is prepared using FIB-INLO, the microstructure of the TBCs can be

analyzed using TEM and STEM techniques. In this study, a Philips/FEI Tecnai F30 300KeV TEM, equipped with high angle annular dark field (HAADF) and x-ray energy dispersive spectroscopy (XEDS), was employed to examine the microstructure of the bond coat, TGO, and YSZ in as-coated and thermally cycled TBCs. Fig. 9 presents typical microstructure of as-coated EB-PVD TBC using the traditional (a) bright

field (BF) and (b) high angle annular dark field (HAADF) images. The HAADF image using STEM mode gives compositional contrast (i.e., analogous to backscatter electron imaging) that can be utilized to identify the presence of mixed-oxide zone in the vicinity of interface between YSZ and TGO. These as-coated microstructures can be related to results from PSLS and EIS as well as processing-dependent lifetime of TBCs [20]. Also using TEM, high resolution images via fast-fourier transformed (FFT) diffractograms can readily identify phase constituents and their crystal structures as presented in Fig. 10 [18]. Fig. 11 shows the BF image of thermally cycled EB-PVD TBC near failure with a thick TGO (nearly 8 μm), and the development of extensive decohesion at the YSZ/TGO interface with thermal cycling. No apparent damage was observed at the TGO to bond coat interface as illustrated by high resolution image presented in Fig. 12 [19]. This is an interesting observation since the final spallation failure of TBCs generally involve separation at the TGO/bond interface.

6. Summary

Fundamentals principles governing two developmental non-destructive evaluation (NDE) techniques, namely photostimulated luminescence spectroscopy (PSLS) and electrochemical impedance spectroscopy (EIS) were introduced along with selected results for applications in lifetime prediction and life-remain assessment of TBCs. In addition, TBC specimen preparation for TEM analysis by focused ion beam (FIB) in-situ lift-out (INLO) was demonstrated along with selected microstructural observations, carried out by TEM and STEM. These results can provide better understanding of TBC failure mechanisms and promote more efficient application of TBCs.

Acknowledgements

References

1. R. A. Miller : Thermal barrier coatings for aircraft engines: History and directions, *J. Thermal Spray Technol.*, Vol. 6, (1997), pp. 35-43
2. A. G. Evans, D. R. Mumm, J. W. Hutchinson, G. H. Meier, and F. S. Pettit : Mechanisms controlling the durability of thermal barrier coatings, *Prog. Mater. Sci.*, Vol. 46, (2001), pp. 505-553
3. Y. H. Sohn, J. H. Kim, E. H. Jordan, and M. Gell : Thermal cycling of EB-PVD/MCrAlY thermal barrier coatings : I. microstructural development and spallation mechanisms, *Surf. Coat. Technol.*, Vol. 146, No. 147 (2001), pp. 70-78
4. Y. H. Sohn, E. Y. Lee, B. A. Nagaraj, R. R. Biederman, and R. D. Sisson, Jr. : Microstructural characterization of thermal barrier coatings on high pressure turbine blades, *Surf. Coat. Technol.*, Vol. 146, No. 147 (2001), pp. 132-139
5. R. J. Christensen, D. M. Lipkin, and D. R. Clarke : Nondestructive evaluation of the oxidation stresses through thermal barrier coatings using Cr^{3+} piezospectroscopy, *Appl. Phys. Lett.*, Vol. 69, (1996), pp. 3754-3756
6. Q. Ma and D. R. Clarke : Stress measurement in single-crystal and polycrystalline ceramics using their optical fluorescence, *Journal Am. Ceram. Soc.*, Vol. 76, (1993), pp. 1433-1440
7. Y. H. Sohn, K. Vaidyanathan, M. Ronski, E. H. Jordan, and M. Gell : Thermal cycling of EB-PVD/MCrAlY thermal barrier coatings: II. Evolution of photostimulated luminescence, *Surf.*

Coat. Technol., Vol. 146, No. 147 (2001), pp. 102-109

8. D. M. Lipkin, H. Schaffer, F. Adar, and D. R. Clarke : Lateral growth kinetics of α-Alumina accompanying the formation of a protective scale on (111) NiAl during oxidation at 1100°C, Appl. Phys. Lett., Vol. 70, (1997), pp. 2550-2552

9. Q. Wen, D. M. Lipkin, and D. R. Clarke : Luminescence characterization of chromium -containing θ-Alumina, Journal Am. Ceram. Soc., Vol. 81, (1998), pp. 3345-3348

10. A. A. Kaplyanski, A. K. Przhevuski, and R. B. Rozenbaum : Deformational splitting of luminescence spectral lines and the structure of exchange linked pairs of chromium ions in ruby, Sov. Phys. Solid State, Vol. 10, (1969), pp. 1864-1869

11. Y. H. Sohn, K. Schlichting, K. Vaidyanathan, E. Jordan, and M. Gell : Communication: non-destructive evaluation of residual stress in thermal barrier coated turbine blades by Cr^{3+} photoluminescence piezo-spectroscopy, Metall. Mater. Trans. A, Vol. 31A, (2000), pp. 2388-2391

12. D. R. Clarke, R. J. Christensen, and V. K. Tolpygo : The evolution of oxidation stresses in zirconia thermal barrier coated superalloys leading to spalling failure, Surf. Coat. Technol., Vol. 94, No. 95 (1997), pp. 89-93

13. B. Jayaraj, S. Vishweswaraiah, V. H. Desai, and Y. H. Sohn : Electrochemical impedance spectroscopy of thermal barrier coatings as a function of isothermal and cyclic thermal exposure, Surf. Coat. Technol., (2004) in Press

14. S. Vishweswaraiah, B. Jayaraj, Y. H. Sohn, T. Du, and V. H. Desai : Non-destructive evaluation of thermal barrier coatings by electrochemical impedance spectroscopy, in thermal spray 2003: Advancing the science and applying the technology, eds. B. R. Marple and C. Moreau, ASM International, (2003), pp. 1487-1494

15. B. Jayaraj, V. H. Desai, C. K. Lee, and Y. H. Sohn : Electrochemical impedance spectroscopy of porous ZrO_2 - 8 wt.% Y_2O_3 and thermally grown oxide on Nickel Aluminide, Mater. Sci. Eng. A, (2004) in Press

16. A. Conde and J. J. de Damborenea: Electrochemical impedance spectroscopy for studying the

degradation of enamel coatings, Corr. Sci., Vol. 44, (2002), pp.1555-1567

17. R. de Levie : On impedance measurements : The determination of the double layer capacitance in the presence of an electrode reaction, Electrochim. Acta, Vol. 10, (1965), pp. 395-402

18. S. Laxman, B. Franke, B. W. Kempshall, Y. H. Sohn, L. A. Giannuzzi, and K. S. Murphy : Phase transformation of thermally grown oxide on (Ni,Pt)Al bond coat during electron beam physical vapor deposition and subsequent oxidation, Surf. Coat. Technol., (2004) in Press

19. B. Kempshall, Y. H. Sohn, S. K. Jha, S. Laxman, R. R. Vanfleet, and J. Kimmel : An observation of nearly failed electron beam physical vapor deposited thermal barrier coating with grit blasted (Ni,Pt)Al bond coat : photostimulated luminescence and transmission electron microscopy, Thin Solid Films, (2004) in Press

20. A. Burns, R. Subramanian, B. W. Kempshall, and Y. H. Sohn : Microstructure of As-coated thermal barrier coatings with varying lifetimes, Surf. Coat. Technol., (2004) in Press